energies

Article

Heat-Up Performance of Catalyst Carriers—A Parameter Study and Thermodynamic Analysis

Thomas Steiner [1], Daniel Neurauter [1], Peer Moewius [1], Christoph Pfeifer [2], Verena Schallhart [1] and Lukas Moeltner [1,3,*]

[1] Department for Industrial Engineering and Management, Management Center Innsbruck, 6020 Innsbruck, Austria; thomas.Steiner@mci.edu (T.S.); daniel.neurauter@outlook.com (D.N.); p.moewius@mci4me.at (P.M.); verena.schallhart@mci.edu (V.S.)
[2] Institute for Chemical and Energy Engineering, University of Natural Resources and Life Sciences, 1180 Vienna, Austria; christoph.pfeifer@boku.ac.at
[3] Institute for Powertrains and Automotive Engineering, Vienna University of Technology, 1060 Vienna, Austria
* Correspondence: lukas.moeltner@mci.edu; Tel.: +43-512-2070-4132

Abstract: This study investigates geometric parameters of commercially available or recently published models of catalyst substrates for passenger vehicles and provides a numerical evaluation of their influence on heat-up behavior. Parameters considered to have a significant impact on the thermal economy of a monolith are: internal surface area, heat transfer coefficient, and mass of the converter, as well as its heat capacity. During simulation experiments, it could be determined that the primary role is played by the mass of the monolith and its internal surface area, while the heat transfer coefficient only has a secondary role. Furthermore, an optimization loop was implemented, whereby the internal surface area of a commonly used substrate was chosen as a reference. The lengths of the thin wall and high cell density monoliths investigated were adapted consecutively to obtain the reference internal surface area. The results obtained by this optimization process contribute to improving the heat-up performance while simultaneously reducing the valuable installation space required.

Keywords: catalytic converter; light-off; monolith; cell density; wall thickness; cordierite

Citation: Steiner, T.; Neurauter, D.; Moewius, P.; Pfeifer, C.; Schallhart, V.; Moeltner, L. Heat-Up Performance of Catalyst Carriers—A Parameter Study and Thermodynamic Analysis. *Energies* **2021**, *14*, 964. https://doi.org/10.3390/en14040964

Academic Editor: Jacek Pielecha

Received: 13 January 2021
Accepted: 9 February 2021
Published: 11 February 2021

1. Introduction

Nowadays, air pollution and emissions from internal combustion engines (ICE) are major issues, frequently and controversially discussed. The emissions can be divided into two categories: air pollutants—hydrocarbons (HC), carbon monoxide (CO), nitrogen oxides (NO_x), and particulate matter (PM)—toxic or harmful to human health and the environment; and the products of combustion—hydrocarbons and carbon dioxide (CO_2)—which are not considered harmful but potentially contribute to atmospheric changes. While the extent of CO_2 emitted correlates strongly with the carbon content in fuels and the fuel consumption of ICEs, the generation of emissions can be affected by combustion properties. To meet emission level requirements, internal measures regarding excess air, exhaust gas recirculation, or complex injection and ignition strategies become less effective. Furthermore, these measures generally reduce the efficiency of ICEs and therefore increase CO_2 emissions. In light of this conflict of objectives, exhaust gas after-treatment systems become the focus of attention. Exhaust gas after-treatment or emission control refers to those systems located downstream of the engine—catalytic converters, sensors, particulate filters, and auxiliary systems—whose primary function is to reduce engine emissions [1]. In exhaust gas after-treatment heterogeneous catalysis is a very effective and commonly used method to reduce gaseous emissions, irrespective of the engine type, either spark-ignited (SI) or compression-ignited (CI).

Since heterogeneous catalysis is a surface reaction, a large internal surface area of the catalytic converter is required to reduce emissions and meet installation space requirements effectively. At present, the most commonly applied converters in passenger vehicles, depending on the engine type, are three-way catalytic converters (TWC), diesel oxidation catalytic converters (DOC), nitrogen oxide storage converters (NSC), and selective catalytic reduction converters (SCR). The following listing provides a brief description of the mentioned catalytic converter technologies:

- Three-Way Catalytic Converter: TWCs represent an efficient, safe and reliable method for exhaust gas cleaning in SI engines and are operated within a narrow air-to-fuel ratio window, near stoichiometric conditions. The basic functionalities of a TWC can be described as follows: oxidation reactions of HC and CO and reduction reactions of NO_x using HC, CO or hydrogen as reductants. Oxidation reactions are primarily catalyzed through platinum group metals, platinum (Pt), and palladium (Pd), while rhodium (Rh) supports the reduction reactions. Furthermore, cerium can act as an oxygen buffer. Light-off temperatures of TWCs are reported to be typically in a range between 548 K, e.g., [2,3] and 573 K, [4]. In stationary engines, the TWC technology is also known as non-selective catalytic reduction (NSCR).
- Diesel Oxidation Catalyst: The main function of DOCs is the oxidation of HC, CO and partly of particulate matter (PM), in lean-burn engines such as diesel engines. In addition, DOCs are employed to control the nitrogen dioxide (NO_2) share in the exhaust gas to support the continuous regeneration of particulate filters and SCR-reactions. Commonly used catalytically active components are Pt and Pd or a combination of both on Al_2O_3. Due to the installation order, close to the engine, light-off issues are only of minor relevance, in the literature reported light-off temperatures for CO oxidation range from 443 K to 493 K [5].
- Nitrogen Oxide Storage Catalyst: This technology is applied in lean-burn gasoline engines as well as in diesel engines. The functionality of NSC can be divided into two phases: the storage of NO_2 under lean conditions, e.g., on barium oxide, and a subsequent and periodically repeating reduction during rich conditions, e.g., on Rh. Since it is only possible to store NO_2, NO must be oxidized prior storing. The typical activity window of NSCs is between 423 K and 723 K. In a temperature range below 573 K the efficiency of NSCs is essentially determined by the oxidation of NO to NO_2 [5].
- Selective Catalytic Reduction: The SCR of NO_x with ammonia (NH_3) is a widespread solution to meet upcoming emission regulations for lean-burn combustion engines. Due to the toxicity of ammonia, exclusively SCR systems with precursor substances, e.g., urea-water solution, are available or being developed. Ammonia is generated within mixing sections upstream of the converter by two reactions, namely, thermolysis of urea, and hydrolysis of the before formed intermediate isocyanic acid cf. [6]. The determining factors for the efficiency of SCR systems are sufficient ammonia generation, adequate homogenization upstream of the catalytic converter and the converter temperature. Due to the installation position of SCR converters, e.g., downstream a DOC, a particulate filter and a mixing section, the heat economy deserves distinct attention. Catalytically active sites can be copper or iron, which are incorporated in zeolites, or vanadium-based formulations. Operation temperatures for SCR-converters must be commonly between 453 K and 723 K [5,7]. Furthermore, the necessary ammonia generation upstream the converter typically requires a temperature of approximately 473 K cf. [6].

One common property of all catalytic converters can be found in their layout and design, which typically consists of a carrier, mostly a monolithic ceramic support material, a high surface coating material, a washcoat, and catalytically active components—noble or transition metals, which are applied to, or incorporated in the washcoat. Figure 1 (left) illustrates the concept consisting of a square-channeled ceramic carrier ① and washcoat layer ②, in this particular case, a modified zeolite.

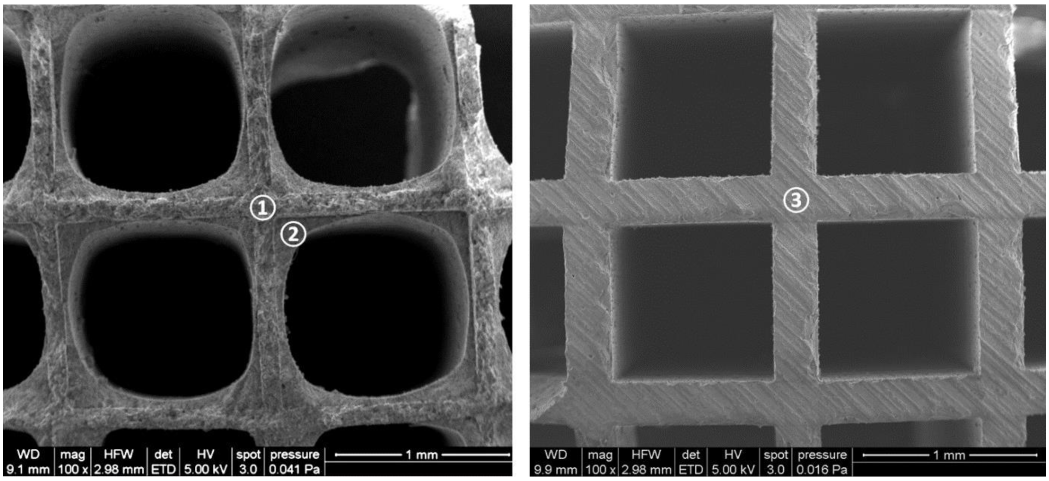

Figure 1. Scanning electron microscope image of an exemplary catalytic converter consisting of: ① a ceramic carrier; and ② washcoat layer; versus a ③ fully extruded converter.

Next to the carrier-supported catalyst concept, there are also full extrudates. This type of catalytic converter is not coated as the extrusion material possesses catalytic properties itself, cf. Figure 1 (right). For the sake of completeness, metallic substrates must also be considered. A more detailed comparison and description is given in Section 3.2.

2. Problem Statement and Scope of this Study

Irrespective of the type of catalytic converter used, these require a specific minimum operation temperature, referred to as light-off temperature. Below this critical temperature, the conversion of pollutants is poor and contributes to relatively high emissions.

Based on this temperature-dependent conversion of pollutants in catalytic converters, two challenges arise: the first challenge here is to keep the period between engine start-up and achieving the light-off temperature as short as possible, and the second task consists of maintaining catalyst temperature above light-off, even at unfavorable operation conditions, such as in phases of idling. The latest developments in European exhaust gas legislation, specifically the expected draft for EURO 7 in 2021, move light-off issues to the focus of interest.

Figure 2 provides an example of temperature-dependent conversion rates of two SCR converters consisting of ion-exchanged zeolites at a space velocity (GHSV) of 20,000 h^{-1} and clearly demonstrates the temperature's significance. Even the copper-containing zeolite with its inherently higher low-temperature activity delivers only limited NO_x conversion at temperatures below 473 K.

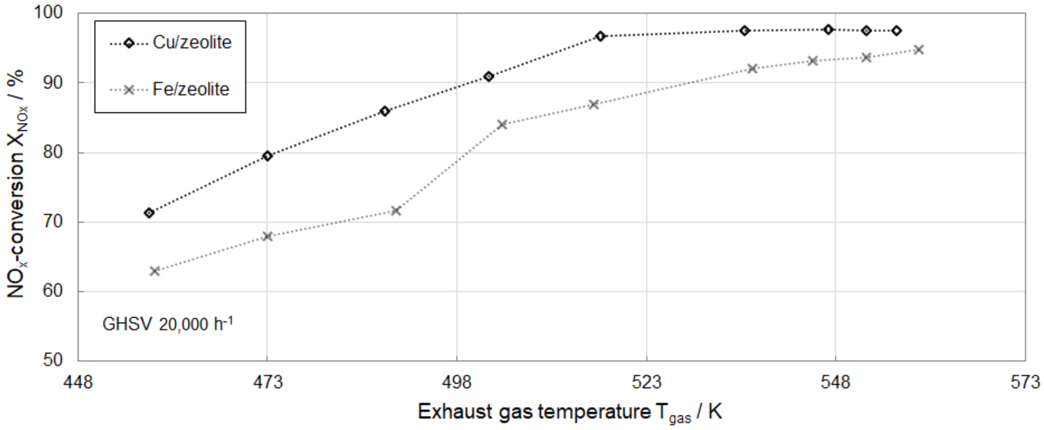

Figure 2. Comparison of conversion rates of two different SCR converters.

Although, the impact of the catalyst substrates' geometric and physical parameters on their heat economy is partially discussed, e.g., in Marsh et al. [8] and Gulati [9], the scope of this study is an in-depth analysis of the heat transfer between exhaust gas and converter. In contrast to other investigations, the present research attempts to determine the influence of all aforementioned parameters on the converter's thermal behavior by means of numerical modeling. For this purpose, a previously developed and published numerical model [1] was adapted and refined to describe the progress of the converter's temperature in the exhaust gas system and to evaluate the advantages and disadvantages of different converter geometries. In terms of efficient heat utilization from the exhaust gas, the results should also serve as decision support for geometric layouts along with possible active heating strategies, e.g., online burners or direct heating of substrates.

3. Literature Review

Strict exhaust gas legislation for motor vehicles requires the use of increasingly efficient concepts for exhaust gas after-treatment. Besides internal measures aiming to reduce engine-out emissions and optimized warm-up strategies for the exhaust gas system, catalytic converter properties play a crucial role. Against this background, internal and external thermal management measures must be applied, such as intake and exhaust throttling, delayed and post-injection strategies for late combustion phasing, cylinder deactivation, high exhaust gas recirculation (EGR) rates, variable valve control/internal EGR, HC dosers, electric exhaust gas heaters, and various non-catalytic or catalytic burner systems, cf. [10–15].

The problematic nature of light-off issues can partly be countered by catalytic coatings featuring distinct low-temperature activation, which, in turn, must also provide adequate conversion at high temperatures after warm-up. Another approach can be found in catalytic converter geometry, which must fulfill two contradicting requirements: for efficient conversion, the converter must deliver a large catalytically active surface while at the same time complying with the generally severely limited installation space calling for a small volume.

At this point, it must be stated clearly that an effective exhaust gas after-treatment system does not follow one individual strategy but consists of all the elements described—internal measures, warm-up strategies, and appropriate catalytic converter [16].

Since this study deals with carrier geometry parameters, the following section describes the respective state-of-the-art design. The list below sums up design targets of catalyst carriers ensuring performance, robustness, and durability of catalytic converter systems, cf. [17–20]:

- large open frontal area (OFA),
- high geometric surface area (GSA),
- low thermal mass/heat capacity,
- thermal stability,
- low coefficient of thermal expansion,
- thermal shock resistance,
- mechanical strength,
- chemical resistance,
- coatability and washcoat compatibility.

3.1. Ceramic Catalyst Substrates

A commonly used material for catalyst carriers and substrates that meets all of these requirements is synthetically manufactured cordierite. Cordierite belongs to the family of silicate ceramics and is produced by using alumina, talc, clay, and silica as raw materials. The manufacturing process is detailed by the respective producer but can be generalized as follows: the raw materials mentioned are crushed and ground, and the resulting powders are mixed with water and several additives. Typical additives are lubricants such as ethylene glycol or oils, binding additives such as methylcellulose, and flux agents such as alkaline hydroxides. After mixing, the paste-like admixture is extruded by piston- or screw extruders. Subsequently, the extruded raw material is cut to the desired length, dried, debindered, and finally sintered at temperatures of approximately 1673 K. The product of this simplified process is referred to as ceramic monolith or honeycomb, cf. [21–23].

In contrast to the cellular monolithic substrates mentioned, non-cellular substrates—rigid foams made of cordierite, silicon carbide, or metal—were also developed, see, e.g., [24,25]. The results published by Jatkar indicate that metallic foams provide a proper support structure for automotive catalysts. Using the foam-supported catalyst with a volume of 0.36 dm^3, the conversion of HC, CO, and NO_x was 90% as efficient as with its conventional ceramic counterpart with a volume of 0.62 dm^3, or a metal foil monolith with a volume of 0.73 dm^3. Although these results are promising, the authors demonstrate the need to further optimize the foam structure and catalyst formulation [26].

The so-called UltraCat™, presented by Stankiewicz et al., consists of an open-cell silicon carbide foam substrate and is particularly designed for fast light-off by incorporating low mass and low heat capacity in a catalyst substrate. The foam exhibits an open frontal area of 87% in a three-dimensionally interconnected open-cell structure [27].

The comparison with cellular substrates presents a relatively small geometric surface area and/or an inadequate high-pressure drop. Therefore, these types of carriers have only found limited commercial use.

With respect to the pressure drop, Lakshmikantha states that the overall pressure drop in catalytic converters is caused by two factors: the nature of inlet and outlet devices and the substrate. The authors identify the substrate as contributing most to exhaust backpressure [28]. In this regard, Pannone et al. describe an estimated loss in power of 300 W per 1000 Pa of extra pressure loss and hereby identify another concern besides light-off issues [29].

Due to the widespread use of non-metric units in the context of describing monoliths' dimensions and to ensure the comparability to other surveys, this study remains consistent with pertinent literature. However, the subsequent paragraph provides an exemplary conversion and dimensions given in Tables 1–3 are in Anglo-American as well as in metric units.

Monolithic catalyst carriers are made of ceramic materials or metals with cell densities from 200 to 1200 cpsi (1 cell per square inch $\hat{=}$ 1550 cells per m^2). The most commonly used cell density for substrates of gasoline and diesel driven vehicles lies between 300–400 cpsi, with a clear trend towards higher cell densities, which provide an increase in the geometric surface area, as noted in [30–32]. Besides the cell density of the monolith, wall thickness also deserves attention as it significantly determines the thermal mass of the substrate and shortens the time for catalyst light-off. A typical wall thickness for monoliths with a cell density of 400 cpsi lies at 4 mil (1 mil $\hat{=}$ 2.54 $\cdot 10^{-5}$ m). In this context, the term ultra-thin wall substrate is frequently used, but it is not unambiguously defined. In some cases, substrates with wall thicknesses below 3.5 mil are classified as ultra-thin wall, while other references define ultra-thin wall substrates with a wall thickness below 2.5 mil [33].

Table 1. Matrix of selected cordierite monoliths to be investigated (●) [10,27].

cpsi **cells·m^{-2}**	**300** **4.65·10^5**	**400** **6.2·10^5**	**600** **9.3·10^5**	**750** **1.16·10^6**	**900** **1.4·10^6**	**1200** **1.86·10^6**
2 mil 50.8 µm	-	-	●	●	●	●
3 mil 76.2 µm	-	●	●	-	-	-
4 mil 101.6 µm	-	●	●	-	-	-
6 mil 152.4 µm	●	●	-	-	-	-
8 mil 203.2 µm	●	-	-	-	-	-

Table 2. Overview of relevant parameter for heat-up at a flow rate of 100 kg/h and 523 K.

Geometries	m/kg	α/W·m^{-2}·K^{-1}	A_{int}/m^2	$t_{Tavg\ 473\ K}$/s	UI/-
300 cpsi, 8 mil 4.65·10^5 cells·m^{-2}, 203.2 µm	1.324	118.61	5.81	38.2	0.942
300 cpsi, 6 mil 4.65·10^5 cells·m^{-2}, 152.4 µm	1.024	114.02	6.05	29.1	0.940
400 cpsi, 6 mil 6.20·10^5 cells·m^{-2}, 152.4 µm	1.172	133.94	6.86	33.1	0.940
400 cpsi, 4 mil 6.20·10^5 cells·m^{-2}, 101.6 µm	0.798	128.12	7.17	22.5	0.940
400 cpsi, 3 mil 6.20·10^5 cells·m^{-2}, 76.2 µm	0.605	125.39	7.32	17.1	0.940
600 cpsi, 4 mil 9.30·10^5 cells·m^{-2}, 101.6 µm	0.968	159.93	8.61	27.2	0.938
600 cpsi, 3 mil 9.30·10^5 cells·m^{-2}, 76.2 µm	0.735	155.70	8.84	20.6	0.937
600 cpsi, 2 mil 9.30·10^5 cells·m^{-2}, 50.8 µm	0.497	151.69	9.08	13.9	0.937
750 cpsi, 2 mil 1.16·10^6 cells·m^{-2}, 50.8 µm	0.554	170.60	10.09	15.5	0.936
900 cpsi, 2 mil 1.40·10^6 cells·m^{-2}, 50.8 µm	0.605	187.90	10.99	16.9	0.935
1200 cpsi, 2 mil 1.86·10^6 cells·m^{-2}, 50.8 µm	0.695	219.12	12.56	19.3	0.934

Table 3. Overview of relevant parameter for the adapted monoliths.

Geometries	l_{mono}/inch, l_{mono}/m	m/KG	A_{int}/m^2 (const.)	$t_{Tavg\ 473\ k}$/ S	UI/-
400 cpsi, 4 mil 6.20·10^5 cells·m^{-2}, 101.6 µm	6.00 0.152	0.798	7.17	22.5	0.940
600 cpsi, 4 mil 9.30·10^5 cells$^{\cdot m-2}$, 101.6 µm	5.00 0.127	0.806	7.17	22.7	0.939
600 cpsi, 3 mil 9.30·10^5 cells·m^{-2}, 76.2 µm	4.86 0.124	0.596	7.17	16.8	0.939
600 cpsi, 2 mil 9.30·10^5 cells·m^{-2}, 50.8 µm	4.74 0.120	0.392	7.17	11.0	0.939
750 cpsi, 2 mil 1.16·10^6 cells·m^{-2}, 50.8 µm	4.27 0.108	0.393	7.17	11.1	0.938
900 cpsi, 2 mil 1.40·10^6 cells·m^{-2}, 50.8 µm	3.92 0.099	0.395	7.17	11.1	0.937
1200 cpsi, 2 mil 1.86·10^6 cells·m^{-2}, 50.8 µm	3.42 0.087	0.397	7.17	11.1	0.937

As mentioned above, thin wall thicknesses accompanied by high cell densities deliver a high geometric surface area and small overall heat capacity, also referred to as thermal mass. Tracing this approach, Twigg convincingly describes the reduction of light-off time as the key parameter in achieving very low emissions [34].

Tanaka et al. highlight a similar approach by focusing on lightweight substrates with wall thicknesses of 2 mil and 3 mil. The authors describe the development of a substrate with strong and stiff walls in the outer region to increase isostatic strength. This is achieved by ensuring that the outermost cells of the substrate are thicker than the inner cells [35].

Umehara et al. also discuss results from catalyst light-off testing on an engine dynamometer and compare these with theoretical results for ultra-thin wall ceramic substrates. The results show that thermal mass has the greatest effect on light-off performance. The authors explicitly state that higher cell density per se provokes extra thermal mass, and the greatest benefit can be found in a reduced wall thickness [36].

In their research, Lafyatis et al. describe how thin wall substrates offer lower thermal mass and better heat transfer properties for faster light-off and better mass transfer characteristics for increased performance. This study investigates the behavior of high cell density substrates by means of numerical and experimental methods. A comparison of 400 cpsi/6 mil, 600 cpsi/4 mil, 600 cpsi/3 mil, and 900 cpsi/2 mil was carried out and presented significant advantages for the 900 cpsi/2 mil substrate [37].

The contribution of Wiehl et al. presents ceramic monoliths featuring cell densities of 600, 900, and 1200 cpsi with wall thicknesses between 2–3.5 mil. Essentially, this study sums up similar advantages and challenges as do the studies mentioned, although a further-reaching approach can be found in a possible reduction of the converter volume achieved by the increased geometric surface area [16]. Independently, Hirose et al. refer to this strategy of reducing the catalyst's volume by increasing the geometric surface area as "downsizing" [38].

Several other studies deal with the interaction between cell density, wall thickness, and converter performance. In sum, these studies determine that high cell densities lead to a large geometric surface area but, in turn, are associated with an increase in pressure drop. They suggest that an increase in cell density should be accompanied by a reduction in wall thickness to compensate for the increased pressure drop. Furthermore, manufacturing costs and mechanical strength are taken into account and identified as critical factors in [39–41].

Anderson follows the move towards ultra-thin wall substrates from another perspective and presents challenges in packaging. As to mounting mats, two main problems with conventional intumescent mats are addressed: first, the intumescent mats generate too much pressure during the assembly process, which can lead to a collapse of substrates during assembly; second, pressure peaks occur in heated intumescent mats, possibly causing broken substrates in vehicles [42].

3.2. Metal Catalyst Substrates

In addition to ceramic support materials, carriers made of wound thin metal foils are also commercially available. Another difference between ceramic and metal carriers can be found in the respective cell geometry. Since ceramic carriers mostly feature square channels (triangular, hexagonal, trapezoidal, and circular channels are also possible), metal substrates can generally be equipped with a sinusoidal channel cross-section and generally offer significant degrees of freedom of design [43].

Bonnefoy et al. investigate pre-coated metallic foils with a thickness of 50 µm, which are welded to a metallic frame and form a substrate block. This approach results in high design flexibility permitting the use of high cell density substrates up to 1250 cpsi without any significant drawbacks in pressure drop [44]. Kikuchi et al. follow the same approach and apply improved high cell density and lightweight substrates. The authors also report on the availability of 1000 cpsi monolith made of ceramic or metal [45].

A present and inherent drawback of metal carriers is their higher cost compared to ceramic counterparts, which negatively affects their wide acceptance.

4. Methodology

This section provides an overview of the chronological sequence of investigations and presents materials and methods applied. The first part compares a geometric parameter study of several monoliths and parameters such as the mass of monoliths, their geometric surface area, and their open frontal area. Second, the influence of geometric aspects on heat transfer is discussed. Subsequently, the heat-up performance of several monoliths during constant boundary conditions (exhaust gas temperature and flow rate are constant) is evaluated by a simulation model. The last part of this section investigates the heat-up performance of monoliths whose internal surface area (A_{int}) was adjusted to compare with the internal surface area of a commonly applied reference monolith with a cell density of 400 cpsi and a wall thickness of 4 mil. Figure 3 graphically presents the chronological sequence of investigations.

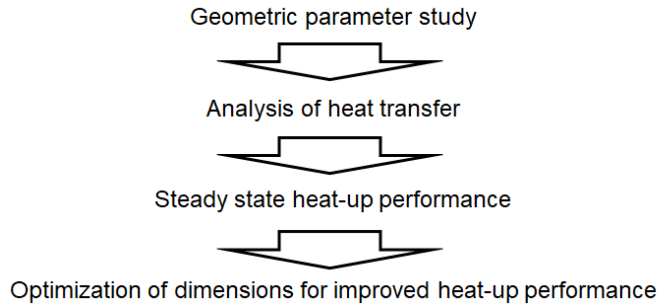

Figure 3. Chronological sequence of investigations.

4.1. Investigated Monoliths

The selection of monoliths was carried out based on their commercial availability and respective literature. With respect to the intended comparative nature of this study, the prevalent standard dimensions of monoliths with 5.66 inch (≙143.8 mm) in diameter and 6 inch (≙152.4 mm) in length were chosen. Table 1 provides an overview of cell densities and wall thicknesses (in Anglo-American as well as in metric units) of the monoliths investigated.

4.2. Simulation Model

The simulation model described by Moeltner et al. in [1] was adapted and applied to the numerical investigation of temperature behavior of SCR catalytic converters under steady state conditions. The heat transfer processes in the exhaust gas system are calculated by two parallel running 1D simulations. Both temperature changes in the pipe wall and catalysts and the change in temperature of the exhaust gas are considered. For the simulation of the temperature change, uniformly distributed cells throughout the exhaust system are used as shown in Figure 4.

The cell size is defined such that an additional reduction in the size has no impact on the accuracy of the results. Additionally, the model is validated by comparing the calculations and empirical data presented in [1].

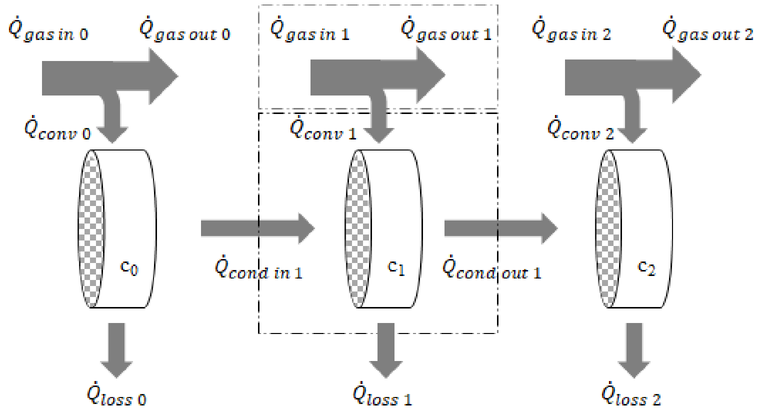

Figure 4. Schematic structure of the chosen simulation strategy.

The temperature development of the exhaust gas (T_{gas}) is determined by the amount of heat emitted or absorbed in one gas cell due to forced convection between the exhaust gas and the after-treatment system ($\dot{Q}_{conv}$). The temperature difference in the gas cell is approximated by the logarithmic mean temperature difference ($\Delta T_{ln\ mean}$), as demonstrated in Equation (1), where the solution of this equation is obtained by an iterative solver, using the Dirichlet boundary condition for the exhaust gas entry. Further variables, which deserve definitions are the gravimetric flow rate of the exhaust gas ($\dot{m}_{gas}$), isobaric heat capacity of the exhaust gas ($c_{p\ gas}$) and the coefficient for convective heat transfer (α).

$$\dot{Q}_{conv} = \dot{m}_{gas} \cdot c_{p\ gas} \cdot \Delta T_{gas} = \alpha \cdot A_{int} \cdot \Delta T_{ln\ mean} \quad (1)$$

The heat balance for one solid cell, with its mass (m_{solid}), consists of the conductive heat transfer between the individual solid cells ($\dot{Q}_{cond}$), the convective heat transfer between the exhaust gas and the after-treatment system, and heat losses ($\dot{Q}_{loss}$), as shown in Equation (2):

$$\dot{Q}_{conv} = m_{solid} \cdot c_{p_{solid}} \cdot \frac{\mathrm{d}T}{\mathrm{d}t} = \pm \dot{Q}_{cond\ in\ 1} \pm \dot{Q}_{conv\ 1} \pm \dot{Q}_{cond\ out\ 1} - \dot{Q}_{loss\ 1} \quad (2)$$

The time-dependent temperatures for both the solid cells and exhaust gas were determined by solving these equations in MATLAB®, The MathWorks, Inc., Natick, Massachusetts, USA, applying Euler-Cauchy with an interval width of 10^{-3} s. The cell resolution for solid cells was defined as 10^{-4} m. The accuracy of the numerical solution strategy could be proved by experimental validation, previously published in [1].

For evaluation of the heat-up performance under steady state conditions, further simplifications were assumed. Even if these assumptions do not describe reality in its entire complexity, the simplifications listed below do not limit the findings' explanatory power due to the comparative nature of this study. For the simulations, the following assumptions were made:

- The exhaust gas is an ideal gas with properties of dry air, $R_{sp} = 287\ \mathrm{J \cdot kg^{-1} \cdot K^{-1}}$; nevertheless, the temperature dependency of heat conductivity λ_{gas}, heat capacity $c_{p\ gas}$, dynamic viscosity η_{gas}, and density ρ_{gas} is included, see Equations (3)–(6).
- All catalytic converters are placed in adiabatic housing, which implies that the heat losses are neglected and no temperature gradients occur within solid cells.
- Reaction enthalpies are not considered to maintain independence from engine-out exhaust gas compositions.
- Heat conductivity, heat capacity and density of solid cells are constant and present typical values for cordierite: $\lambda_{solid} = 2\ \mathrm{W \cdot m^{-1} K^{-1}}$, $c_{p\ solid} = 1000\ \mathrm{J \cdot kg^{-1} K^{-1}}$ and $\rho_{solid} = 2100\ \mathrm{kg \cdot m^{-3}}$.
- Ambient temperature and initial temperature of solid cells at $t = 0$ s are 293 K and pressure is constant at 101,325 Pa.

$$\lambda_{gas} = -0.37 \cdot 10^{-3} + 0.103 \cdot 10^{-3} \cdot T_{gas} - 4.657 \cdot 10^{-8} \cdot {T_{gas}}^2 \quad (3)$$

$$c_{p\ gas} = 1070.3 - 0.564 \cdot T_{gas} + 1.507 \cdot 10^{-3} \cdot {T_{gas}}^2 - 1.102 \cdot 10^{-6} \cdot {T_{gas}}^3 - 1.4 \cdot 10^{-8} \cdot {T_{gas}}^{-2} \quad (4)$$

$$\eta_{gas} = -3.287 \cdot 10^{-3} + 7.7996 \cdot 10^{-8} \cdot T_{gas} - 4.8801 \cdot 10^{-11} \cdot {T_{gas}}^2 \quad (5)$$

$$\rho_{gas} = \frac{p}{R_{sp} \cdot T_{gas}} \quad (6)$$

The stated equations, Equations (3)–(5), are valid for moderate pressures below 500,000 Pa and temperatures in the range from 223 K to 773 K [46]. Regarding the interplay between viscosity, heat conductivity, heat capacity and pressure, it is necessary to mention that the viscosity and heat conductivity of ideal gases can be derived by kinetic gas theory. In detail, the mean free path length increases to the same extent as the density declines with decreasing pressure. Therefore, the viscosity and heat conductivity of (not greatly diluted) ideal gases are independent from pressure within a broad range. In addition, it can be assumed that due to the comparably low particle densities of ideal gases, atoms or molecules are not limited in their molecular motion, thus, the heat capacity is widely independent from pressure.

5. Discussion of Results

This section first provides a brief discussion of differences in geometric and physical properties—mass or geometric surface area and open frontal area of monoliths. Second, it presents a detailed analysis of heat transfer between the exhaust gas and the monoliths, followed by a description of numerical heat-up experiments, which sum up the insights of geometric and physical properties and thermodynamic aspects.

5.1. Geometric Parameter Study

Because of its determining role in the overall heat capacity, which is directly proportional to the mass and delays the heat-up, the first parameter to be contrasted is the mass of the monoliths. As to be expected, this increases indirectly proportionally to the wall thickness and the increase in material. This trend can be traced by considering monoliths with the same cell densities—400 cpsi or 600 cpsi and varying wall thicknesses—as depicted in Figure 5.

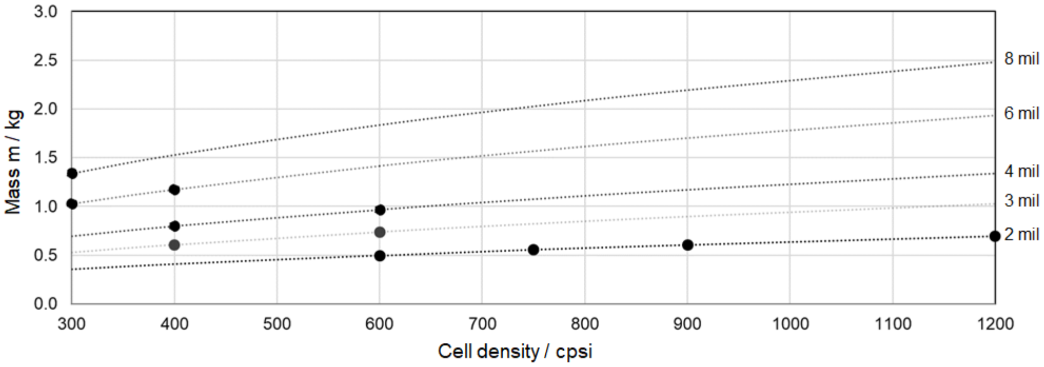

Figure 5. Mass of monoliths with respect to their cell density and wall thickness.

A similar argument applies to the open frontal area (OFA) in percentages. The OFA is defined as the ratio between the monolith's free cross-section and the overall circular cross-section. This can be flowed by the exhaust gas and is a determining factor in the pressure drop over the converter (Figure 6). From the perspective of a minimized pressure drop, the highest possible OFA that can be delivered by substrates with thin wall thicknesses would be desired. A critical comparison between substrates with cell densities of 600 cpsi and higher clearly shows that an increase in cell density at constant wall thicknesses reduces the OFA.

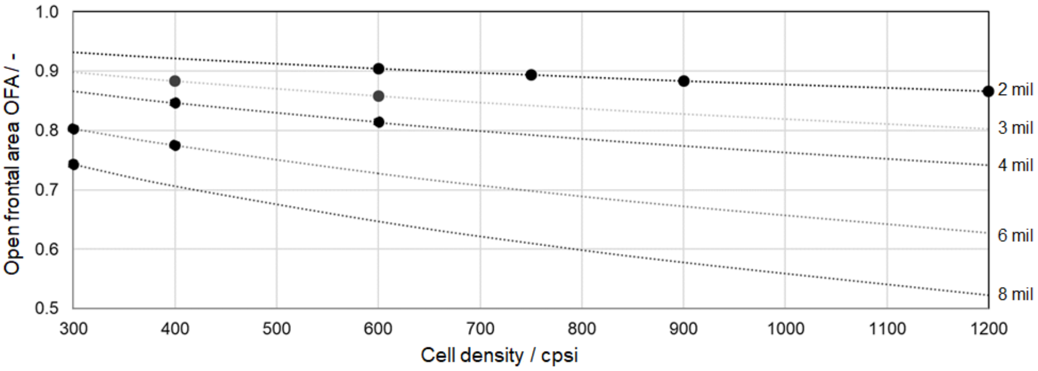

Figure 6. Open frontal area of monoliths with respect to their cell density and wall thickness.

A possible solution with the goal of reducing the time required for monolith heat-up might be found in reducing the mass and simultaneously increasing the OFA. Nevertheless, this argumentation is incomplete since heterogeneous catalysis is a surface reaction, mainly limited by the available surface and the number of catalytically active sites. In this context, the so-called geometric surface area (GSA) also has a significant role in describing the ratio between the monolith's internal surface area and the cylindrical volume of the substrate. When aiming to achieve the largest possible internal surface area that can be coated or possesses incorporated active sites, Figure 7 reveals clear advantages for monoliths with high cell densities—750, 900, and 1200 cpsi.

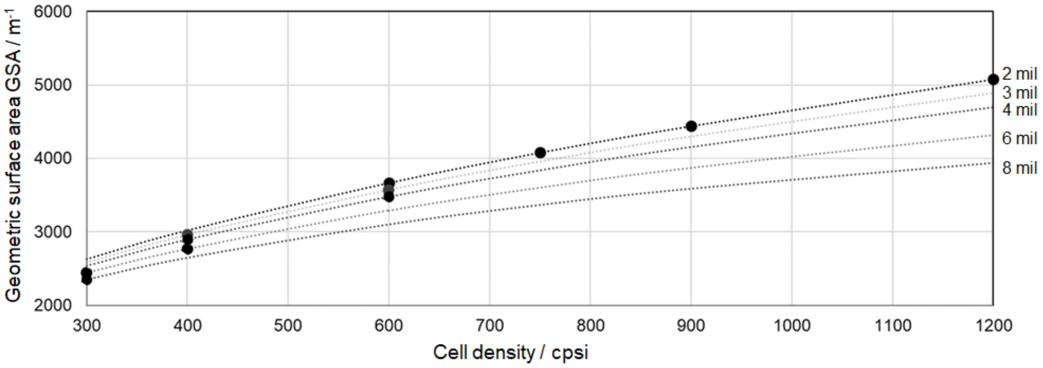

Figure 7. Geometric surface area of monoliths with respect to their cell density and wall thickness.

Irrespective of this advantageous property of high density substrates, the thin wall thicknesses inherently generate higher structural loads for the ceramic material and require greater effort during manufacturing because of the required prevention of crack formation and mechanical collapse.

In sum, it can be stated that high cell densities generate small drawbacks in OFA but have the potential to increase GSA and decrease the mass of a monolith as well as its heat capacity. A compromise is delivered by 600 cpsi substrates, particularly by monoliths with thin wall thicknesses of 2 mil or 3 mil, which present relatively balanced properties regarding the parameters discussed.

5.2. Thermodynamic Analysis

This subsection provides a detailed analysis of the thermal interaction between exhaust gas and monoliths in varying dimensions. Equation (7) specifies the extent of convective heat transfer from the exhaust gas to the corresponding internal surface area A_{int} of the monolith. The underlying strategy is based on the determination of the convective heat transfer ($\dot{Q}_{conv}$) in one single channel and a subsequent scale-up in the surface caused by a multitude of channels. Given the fact that the monolith temperature lies below the temperature of the exhaust gas, the monolith experiences a heat input significantly determined by the heat transfer coefficient α and the surface of heat exchange A_{int}:

$$\frac{\mathrm{d}Q_{conv}}{\mathrm{d}t} = \alpha \cdot A_{int} \cdot \mathrm{d}T \tag{7}$$

The role of the internal surface area A_{int}, particularly in hosting catalytically active sites, was previously discussed. Yet, another important aspect is considered in Equation (7). The surface on which convective heat transfer occurs is identical to that used for catalysis. Therefore, its extent can be determined by the GSA. At this point, it can be concluded that monoliths featuring a large GSA supply a large surface area for heat exchange.

Another factor influencing heat transfer is the heat transfer coefficient α, which can individually be determined by the geometric boundary conditions and fluid properties. With an internally flowed square-channeled geometry, the heat transfer coefficient can be calculated using the Nusselt number (Nu), the heat conductivity of the involved gas λ_{gas} and the hydraulic diameter (d_{hydr}) (see Equation (3) and Equation (8)) [47]:

$$\alpha = \frac{Nu \cdot \lambda_{gas}}{d_{hydr}} \tag{8}$$

The Nusselt number Nu is a dimensionless coefficient based on the theory of similarity, which finds broad application in describing convective heat transfer. The calculation of Nu depends on the prevailing flow field. Consequently, the Reynolds number Re, which represents the ratio between inertia forces and viscosity, must be determined beforehand, cf. Equation (9) [47]. Further variables applied are the linear velocity of the exhaust gas in the monolith (u), the exhaust gas density (ρ_{gas}), the hydraulic diameter (d_{hydr}) and dynamic viscosity (η_{gas}):

$$Re = \frac{u \cdot \rho_{gas} \cdot d_{hydr}}{\eta_{gas}} \tag{9}$$

The linear velocity u is determined using the OFA, the circular cross-section of the monolith and the thermic state equation of ideal gases. Figure 8 represents the monolith-dependent flow velocities at an exhaust gas flow rate of 100 kg/h and a temperature of 523 K. These exhaust gas conditions represent a typical low-load operation point of four to six-cylinder engines applied in passenger vehicles.

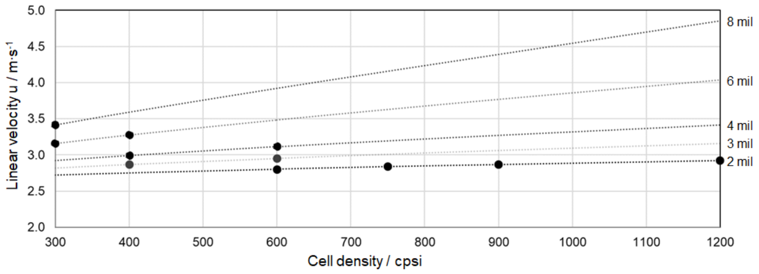

Figure 8. Linear gas velocity at a flow rate of 100 kg/h and 523 K.

Obviously, the flow velocity corresponds directly to the OFA, which means that the reason for increased flow velocities can be found in decreased OFAs and vice versa.

Apart from flow velocity, the determination of the Reynolds number includes the dynamic viscosity (Equation (5)) and density (Equation (6)) of the exhaust gas, as well as the hydraulic diameter d_{hydr} of the channel gained by the free edge length (a), cf. Equation (10) [47]. To support the present discussion, Figure 9 graphically summarizes the hydraulic diameters for all substrates investigated:

$$d_{hydr} = \frac{2 \cdot a^2}{2a} \tag{10}$$

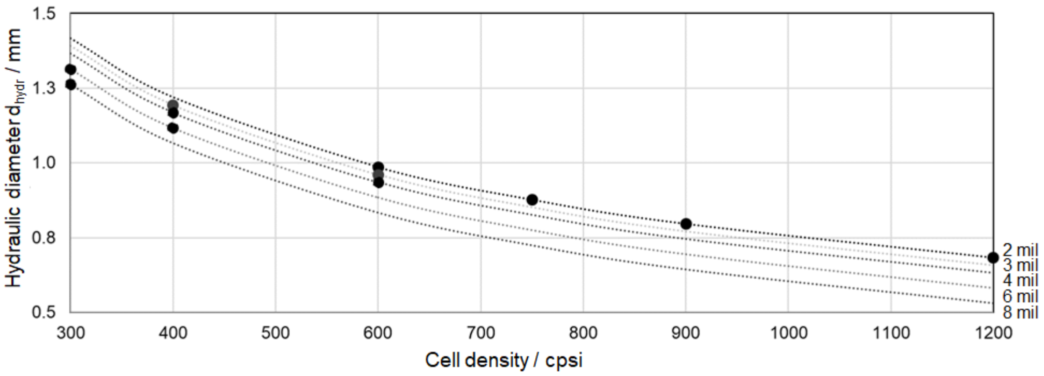

Figure 9. Hydraulic diameters of single channels.

Figure 10 displays the resulting Reynolds numbers, which deliver a preliminary result of interest. Where the Reynolds numbers are far below the transition from laminar ($Re < 2300$) to turbulent flow ($Re > 2300$), Equation (11) comes into force [47]. The relatively short edge length combined with high cell density substrates provokes a decrease in Reynolds numbers. Even the highest Reynolds number indicates a laminar flow field with a decreasing trend in relation to higher cell densities.

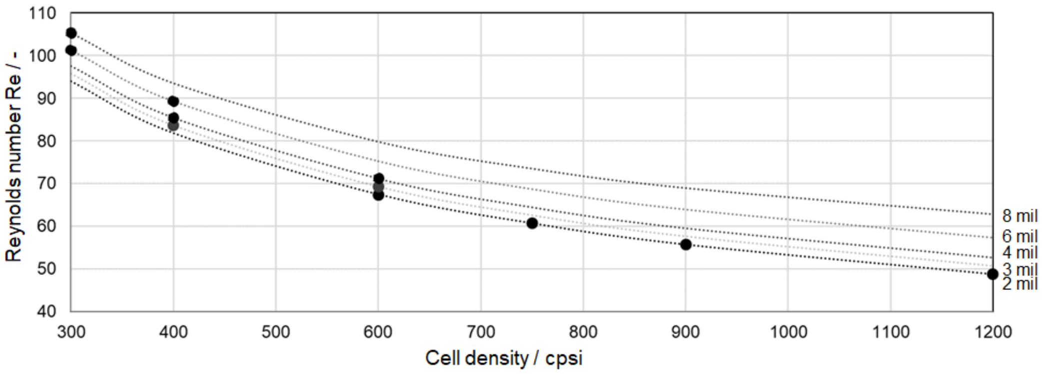

Figure 10. Reynolds numbers at a flow rate of 100 kg/h and 523 K.

The calculation of Nu using Equation (11) presupposes a knowledge of the hydraulic diameter d_{hydr}, the monolith's length l_{mono}, and the Peclet number (Pe), which is defined as the ratio between advective transport and the diffusion rate of a physical quantity used for transport phenomena in the continuum. The Peclet number Pe is the product of Re and the Prandtl number (Pr), Equation (12) [47].

Furthermore, the determination of the Nusselt number requires a case-dependent preselection of equations with respect to the range of validity. For:

- laminar flows with $Re < 2300$,
- Prandtl numbers (Pr) between 0.1 and ∞, and
- $Re \cdot Pr \cdot d_{hydr} \cdot {l_{mono}}^{-1}$ between 0.1 and 10^4, Equation (11) comes into account [47].

$$Nu = \left[3.66^3 + 0.7^3 + \left(1.615 \cdot \left(\frac{Pe \cdot d_{hydr}}{l_{mono}} \right)^{\frac{1}{3}} - 0.7 \right)^3 \right]^{\frac{1}{3}} \tag{11}$$

$$Pe = Re \cdot Pr \tag{12}$$

The Prandtl number Pr combines the velocity pattern of a flow field and the temperature field. Generally, Pr is defined to be the ratio of kinematic viscosity to temperature conductivity. Replacing kinematic viscosity by dynamic viscosity and expressing temperature conductivity by heat capacity and heat conductivity of the exhaust gas delivers Equation (13) [47]:

$$Pr = \frac{\eta_{gas} \cdot c_{p\ gas}}{\lambda_{gas}} \tag{13}$$

Insertion into the respective and previously mentioned equations and the inclusion of the open area of the substrate (A_{open}) finally delivers the heat transfer coefficient (α) for all monoliths investigated (Equation (14)):

$$\alpha = \left[49.37 + \left(1.615 \cdot \left(\frac{\dot{m}_{gas} \cdot c_{p\ gas} \cdot {d_{hydr}}^2}{l_{mono} \cdot A_{open} \cdot \lambda_{gas}} \right)^{\frac{1}{3}} - 0,7 \right)^3 \right]^{\frac{1}{3}} \cdot \frac{\lambda_{gas}}{d_{hydr}} \tag{14}$$

Figure 11 graphically represents the heat transfer coefficients of the substrates investigated at the given flow rate and constant exhaust gas temperature. To interpret these results, it can generally be assumed that all gas properties remain constant due to a constant temperature of 523 K. Thus, all exhaust gas-related numbers remain unaltered—in this case, the Prandtl numbers.

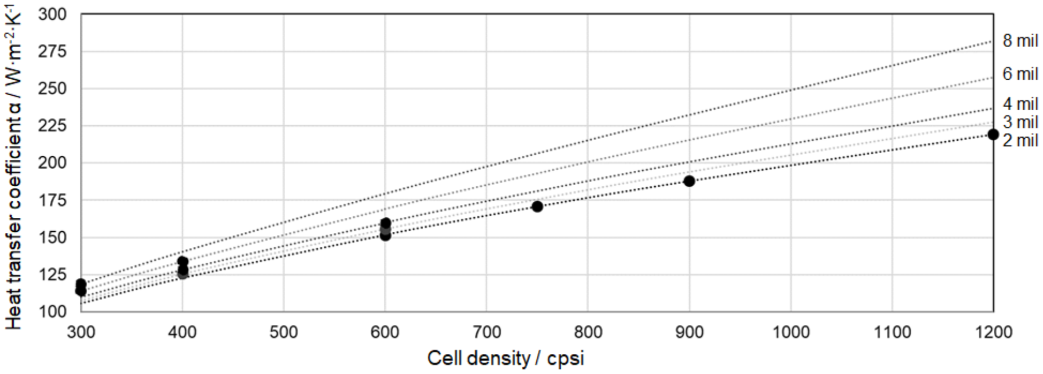

Figure 11. Heat transfer coefficients at a flow rate of 100 kg/h and 523 K.

Consideration of Figure 11 allows us to claim that the three ultra-thin wall substrates with cell densities from 750–1200 cpsi possess the highest heat transfer coefficients. The suppressive effect in terms of heat transfer, caused by small hydraulic diameters resulting in small Reynolds numbers and consequently in decreasing in Nusselt numbers, is compensated by dividing through the hydraulic diameter in Equation 8. In sum, the effect of significantly reduced Reynolds numbers provoked by the short edge length of high-density substrates—750, 900, and 1200 cpsi—does not negatively affect the heat transfer coefficient.

5.3. Steady State Heat-Up

This section describes the monoliths' thermal response during a steady state heat-up phase. The substrates are perfused by a constant mass flow of exhaust gas of 100 kg/h with a temperature of 523 K. Even if this virtual set-up does not mirror real driving conditions, it does allow a detailed analysis of heat transfer and thus identification of critical parameters.

For a comprehensive overview, the following diagrams show temperature change within the substrates, categorized with respect to their cell densities. Figure 12 graphically presents the temperature change within 300 cpsi monoliths with a wall thickness of 8 mil (top) and 6 mil (bottom). The abbreviation c_1 represents the converter entry cell and c_{150} the exit cell with respect to the flow direction. Parameters considered key indicators are the (arithmetic) mean temperature of the monolith ($T_{cat\ avg}$) and the uniformity index (UI), describing longitudinal temperature distribution according to Equation (15):

$$UI = 1 - \frac{\sum_{i=1}^{n} \sqrt{\left(T_{cat(i)} - T_{cat\ avg}\right)^2}}{2 \cdot T_{cat\ avg} \cdot n} \tag{15}$$

The comparison of these diagrams reveals clear advantages in heat-up for the substrate with a wall thickness of 6 mil over 8 mil. For both monoliths, we can attest that the temperature progressively increases from the entrance of the substrate towards the exit. The 8 mil substrate exhibits a slower heat-up because of its higher mass (Figure 5), which cannot be compensated for by slightly higher Reynolds numbers (Figure 10) and therefore increased heat transfer coefficients (see Figure 11). These results agree with the findings of Umehara et al., which make wall thickness primarily responsible for higher thermal mass and slower heat-up [36]. Additionally, we should mention that the 8 mil monolith has the smallest OFA of all substrates, which may provide backpressure disadvantages.

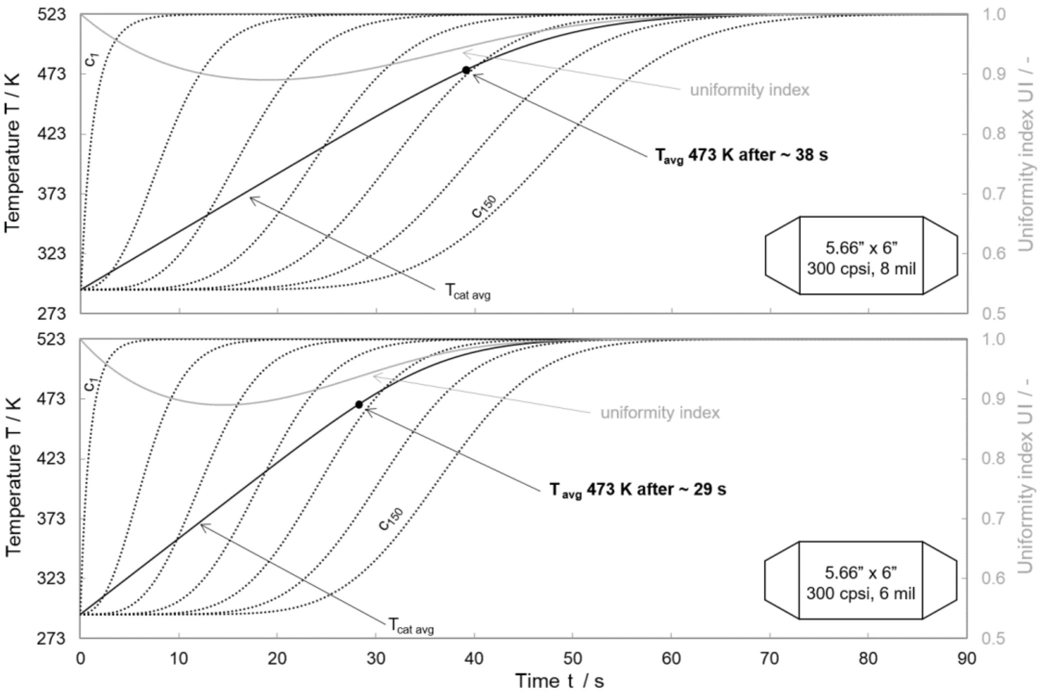

Figure 12. Steady state heat-up of 300 cpsi monoliths at a flow rate of 100 kg/h and 523 K.

A similar tendency is revealed by comparing monoliths with a cell density of 400 cpsi and varying wall thicknesses (Figure 13). The 3 mil substrate exhibits the fastest heat-up in contrast to its 400 cpsi counterparts. The reason can be found in the substrates' varying masses and different thermal inertias. In accordance with the trends discussed in the previous paragraph, the monoliths with greater wall thicknesses provoke higher linear velocities of the exhaust gas within the channels (Figure 8), causing increased Reynolds numbers (see Figure 10) and higher heat transfer coefficient (Figure 11). This gain in heat transfer coefficient cannot offset the drawbacks determined by the higher mass of monoliths with increased wall thicknesses (see Figure 5).

The range of wall thicknesses for commercially available 600 cpsi substrates delivers similar findings to those of 300 cpsi and 400 cpsi monoliths (see Figure 14). The interplay between heat transfer coefficient, (thermal) mass, and internal surface area results again in the shortest heat-up periods for the least wall thicknesses within the same cell density.

The last variation in this comparison focuses on alterations in cell densities by simultaneously keeping the wall thickness constant, as primarily presented in Figure 15. This comparison can be extended to the 600 cpsi monolith with 2 mil given in Figure 14 since the wall thickness is equal. We notice that the heat-up phase is prolonged by increasing cell densities. Within the 2 mil monoliths, the 600 cpsi substrate exhibits the fastest heat-up, although the internal surface area and the heat transfer coefficient are smaller than with higher cell densities. This behavior requires a more detailed analysis and is discussed in the subsequent paragraphs.

Table 2 first summarizes the most significant parameters determining the heat-up duration—the mass of the monolith, an exemplary heat transfer coefficient for a gas temperature of 523 K and a flow rate of 100 kg/h, and the internal surface area A_{int}. Furthermore, this table presents the time required to achieve an average temperature of 473 K ($T_{avg\ 473\ K}$) over all solid cells and the uniformity index, which represents the homogeneity of temperature.

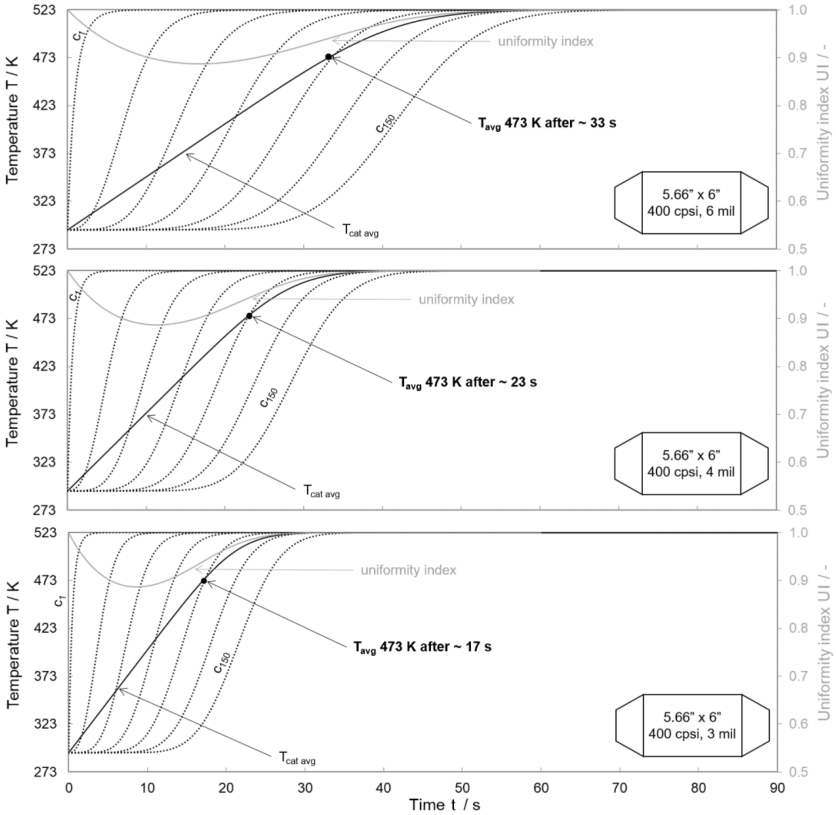

Figure 13. Steady state heat-up of 400 cpsi monoliths at a flow rate of 100 kg/h and 523 K.

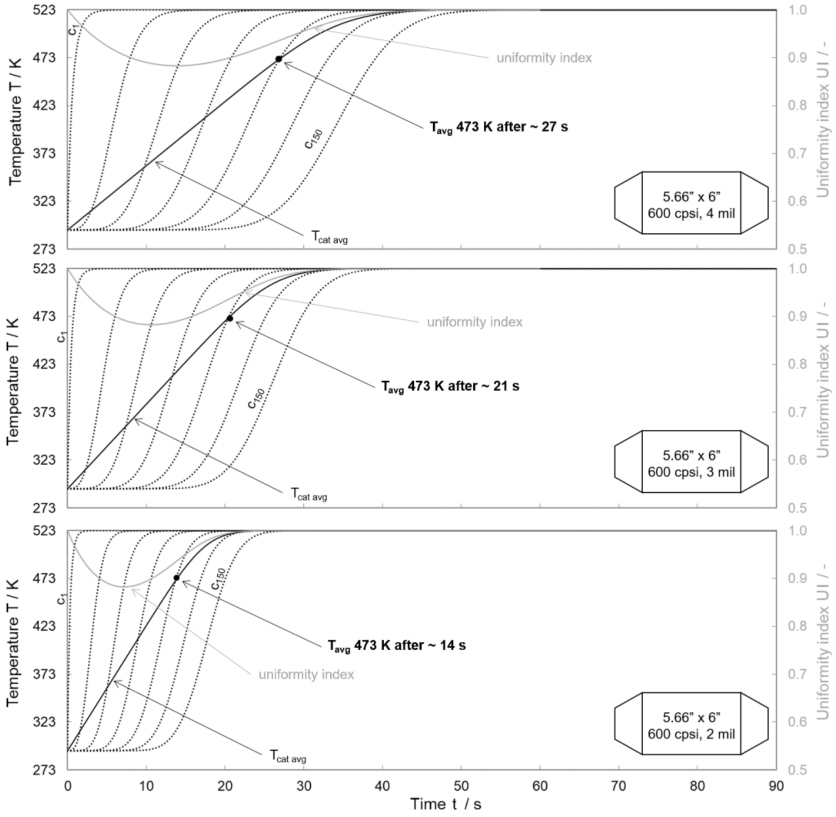

Figure 14. Steady state heat-up of 600 cpsi monoliths at a flow rate of 100 kg/h and 523 K.

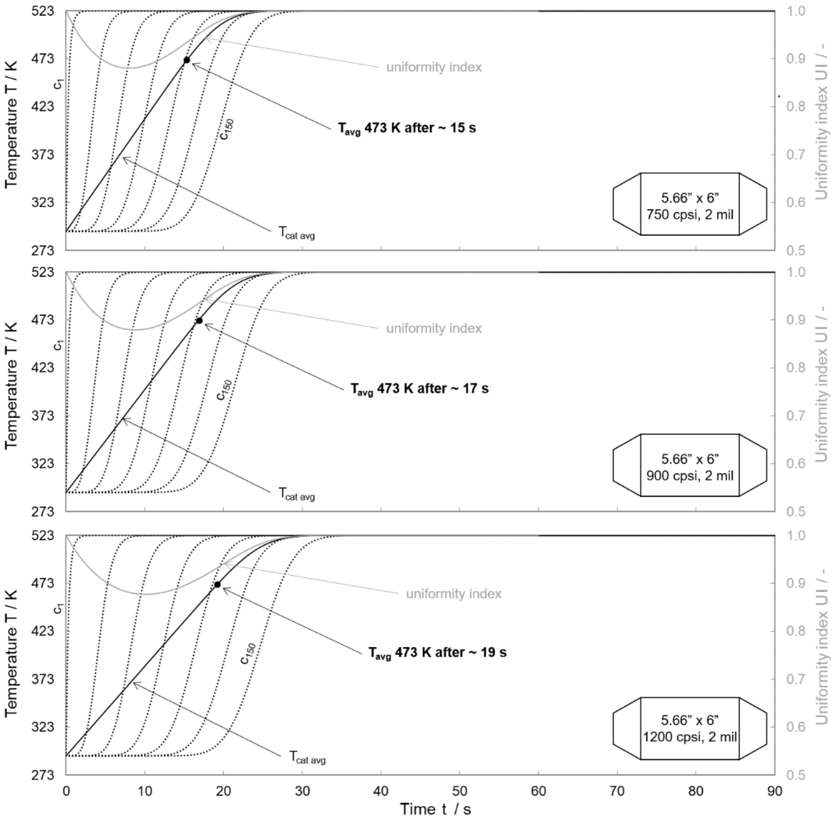

Figure 15. Steady state heat-up of monoliths with 2 mil at a flow rate of 100 kg/h and 523 K.

A critical consideration requires a more detailed analysis of the 2 mil monoliths because smaller cell densities provide shorter heat-up phases than high cell densities. This behavior is exemplified by the comparison of the 600 cpsi substrate, which exhibits a significantly faster heat-up in contrast to its 1200 cpsi counterpart. Comparing Figure 14 (bottom), Figure 15 (bottom) and Table 2 confirms this. This result deserves a more profound thermodynamic analysis since the 1200 cpsi substrate possesses a significantly higher heat transfer coefficient compared to the 600 cpsi monolith (219 $W{\cdot}m^{-2}{\cdot}K^{-1}$ versus 152 $W{\cdot}m^{-2}{\cdot}K^{-1}$, exemplified in Figure 11) as well as a considerably increased internal surface area of 12.56 m^2 for 1200 cpsi over 9.08 m^2 for 600 cpsi. In contrast to these heat transfer-supporting factors, only a minor gain in mass—from 0.497 kg for 600 cpsi to 0.695 kg for 1200 cpsi—is evident.

The thermodynamic examination is supported by Figure 16, which presents the gas temperature at the inlet ($T_{gas\ in}$) and outlet of the monoliths ($T_{gas\ out}$), the convective heat flux ($\dot{Q}_{conv}$), and the average temperature of the substrate for both 600 cpsi and 1200 cpsi with a wall thickness of 2 mil.

In the first seconds, both monoliths completely absorb the convective heat flux generated by the exhaust gas. This effect can be traced by considering $T_{gas\ out}$, which remains constant at the initial temperature (293 K) during this phase, identified as "full heat absorption". The convective heat flux continually remains at a high level of approximately 6.51 kW for both monoliths. The origin of this convective heat flux can be found in the heat power, which can be dispersed by the exhaust gas related to the ambient temperature of 293 K (see Equation (16)), where $c_{mp\ gas}$ represents the average isobaric heat capacity of dry air between 523 K and 293 K, 1019 $J{\cdot}kg^{-1}{\cdot}K^{-1}$.

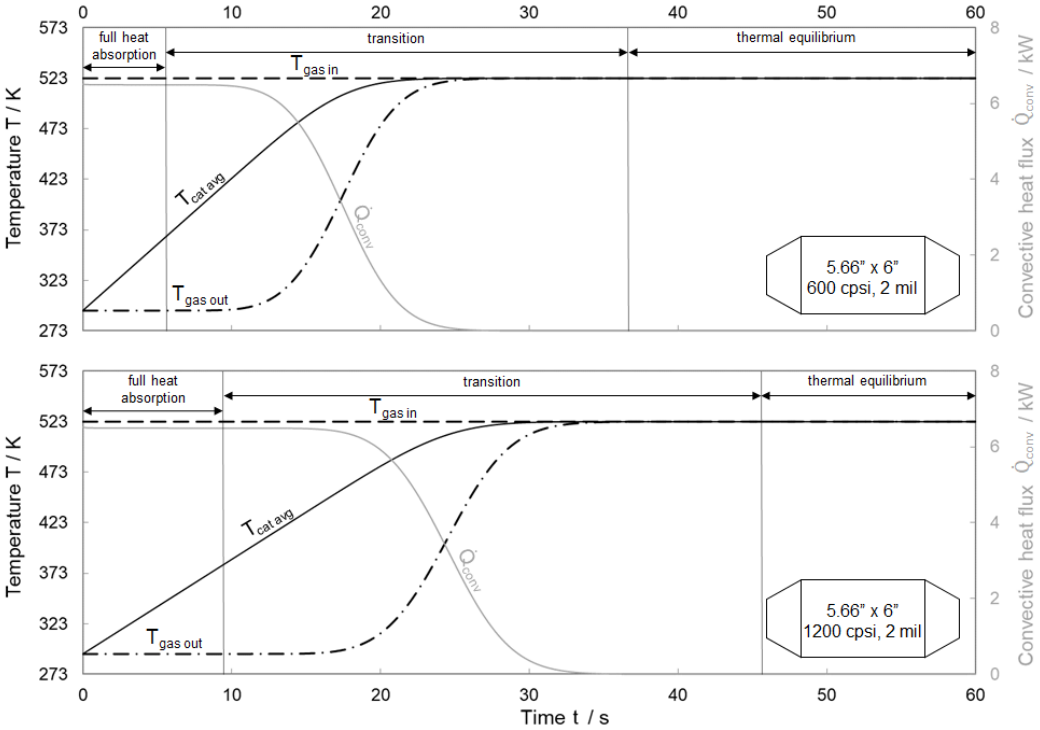

Figure 16. Comparison of 600 cpsi, 2 mil (**top**) and 1200 cpsi, 2 mil (**bottom**) at steady state heat-up at a flow rate of 100 kg/h and 523 K.

$$\dot{Q}_{conv} = \dot{m}_{gas} \cdot c_{mp\ gas} \cdot \Delta T_{gas} = 6.51\ \text{kW} \tag{16}$$

This heat flux, entirely absorbed by the monolith, provokes the change in temperature, Equation (2), which reveals that the change of the monolith's temperature depends exclusively on its mass. The comparison of both periods, described as "full heat absorption" in Figure 16, and the consideration of the monoliths' masses given in Table 2 explain the delayed increase in $T_{cat\ avg}$ and $T_{gas\ out}$ for the 1200 cpsi substrate. This effect of full heat absorption is dependent on a prior condition: the convective heat flux density ($\dot{q}_{conv}$) must be smaller than the convective heat transfer coefficient α, Equation (17):

$$\dot{q}_{conv} < \alpha \tag{17}$$

After this first phase, the exhaust gas at the exit of the substrates increases, and the effect of "full heat absorption" is disabled. The subsequent phase, indicated as "transition," is limited by the intensity of the heat transfer between the exhaust gas and the monoliths' internal surface area. In this period, the interaction between the heat transfer coefficient, the internal surface area, and the mass of the monolith plays the determining role in heat-up. Comparing the (negative) slopes of $\dot{Q}_{conv}$ in Figure 16 reveals that the convective heat flux drops slightly faster with the 600 cpsi monolith than with the 1200 cpsi monolith. This behavior can be identified by tracing the progress of $T_{gas\ out}$. In the 600 cpsi substrate, this temperature increases faster than with the 1200 cpsi monolith. The reason for this can be found in the smaller heat transfer coefficient and smaller internal surface area of the 600 cpsi monolith, which limits convective heat transfer from the exhaust to the substrate more than for the 1200 cpsi substrate; see also heat transfer coefficients and internal surface areas in Table 2. The final phase, indicated as "thermal equilibrium," is characterized by balanced temperatures of the exhaust and the monolith and no further heat transfer occurring. In sum, the higher mass of the 1200 cpsi monolith provokes a longer dwell time in which the supplied heat flux is completely absorbed. The advantages of the 1200 cpsi monolith—a higher heat transfer coefficient and a larger internal surface area—cannot compensate for the initial drawback of the higher mass. The initial lead of the 600 cpsi substrate finally results in a significantly shorter heat-up period compared to its 1200 cpsi counterpart.

5.4. Optimization of Dimensions for Improved Heat-Up Performance

Since heterogeneous catalysis depends significantly on the availability of active sites, the internal surface area plays a dominant role in heat transfer and conversion. The final section of this study exemplarily tests the results gained in the previous sections and describes an adaption of the internal surface area. In detail, the internal surface area of one monolith—400 cpsi with a wall thickness of 4 mil—is set to be the reference due to its prevalent use [33]. The determining variable is the length of the monolith. This decision is based on the practical aspects of manufacturing and tool making. The lengths (l_{mono}) of 600 cpsi, 750 cpsi, 900 cpsi, and 1200 cpsi substrates are reduced in such a way as to create the same internal surface area as the reference mentioned. Table 3 provides an overview of the alterations made in length and reveals the time required to achieve an average monolith temperature of 473 K. With respect to the extent of this study, individual diagrams of the heat-up for the length-reduced monoliths are presented in the Appendix A (see Figures A1–A7 in the Appendix A).

The results given in Table 3 illustrate the decisive role the monoliths' wall thickness has in the heat-up period. With reference to the previous assumption based on an equal internal surface area for the monoliths investigated, the substrate length decreases with increasing cell density. In a group featuring the same wall thickness, the time required for heat-up remains constant. The reason for this behavior can be found in the direct proportionality between the mass and the (absolute) heat capacity and internal surface area. Expressed differently, an increase in cell density while maintaining wall thickness constant does not influence the heat-up time, although it may save installation space.

6. Conclusions

Against the background of increasingly stringent limits to emissions for internal combustion engines, exhaust gas after-treatment plays a crucial role. In terms of light-off issues, the heat-up behavior of catalytic converters is of considerable importance. Given the fact that the exhaust gas convectively heats converters, heat transfer is a dominant issue. Therefore, this study focuses on identifying and quantifying decisive geometric parameters of monoliths—cell density and wall thickness.

The first part of this paper compares geometric properties such as mass, open frontal area, and the geometric surface area for a widely-used dimension in passenger vehicles—5.66″ in diameter and 6″ in length. The cell densities considered range from 300 cpsi–1200 cpsi and the wall thicknesses from 2 mil–8 mil. The prior decision as to which combinations deserve consideration was made with respect to commercially available monoliths. As expected, the geometric surface area greatly depends on cell density, while mass is widely predetermined by wall thickness, and both affect the open frontal area.

Secondly, a thermodynamic analysis was carried out. The extent of the heat transfer coefficient was determined by considering linear velocity, hydraulic diameter, and the Reynolds number for a predefined gas temperature of 523 K and flow rate of 100 kg/h. It can affirm that the hydraulic diameter is the most significant contributing factor to the heat transfer coefficient. The 1200 cpsi monolith with 2 mil wall thickness shows the highest heat transfer coefficient and has the largest internal surface area, which allows us to assume the shortest possible heat-up period in this comparison. In contrast to these properties, consecutively carried out heat-up simulations demonstrate that the 2 mil alternatives with smaller cell density support a faster heat-up period. When the internal surface is considered, this result appears more controversial since the 1200 cpsi monolith possesses the largest internal surface area. To address this apparent conflict, an analysis of convective heat fluxes was included, which supported the effects described.

A quantitative proof provided that the heat flux density from the exhaust gas to the substrate is smaller than the heat transfer coefficient, which results in full heat absorption by the monolith in the first phase of heat-up. During this first phase of full heat absorption, the (thermal) mass of the monolith determines the rise in temperature and explains why the 1200 cpsi monolith suffers a delay compared to its counterparts with smaller cell densities. The second phase of heat-up is not determined by full heat absorption but the heat transfer coefficient and internal surface area. During this phase, the 1200 cpsi substrate surpasses the smaller cell densities but does not have the potential to offset the initial drawbacks during the first phase.

The last part of the investigations presented describes an optimization loop of the monolith's outer dimensions. The length of monoliths selected was reduced in such a way as to achieve the same internal surface area as the 400 cpsi reference monolith with 4 mil in 5.66″ diameter and 6″ in length. It could be shown that the individual reduction in length does not influence the heat-up time as long as the wall thickness remains unchanged. This behavior could be exploited by saving installation space while simultaneously providing short heat-up periods.

Regarding the introductorily stated research question if and how external heating measures can contribute to shorten the warm-up phase, the following findings can be summarized. During the first phase, the converter fully absorbs the provided heat from the exhaust gas and its heat-up performance exclusively depends on its thermal inertia. Therefore, monoliths with high cell densities cannot use their inherent advantages of enhanced internal surface area and increased heat transfer coefficient due to the limited exhaust gas enthalpy. Furthermore, the comparably increased mass for high cell densities (at constant wall thickness) results in higher thermal inertia and act counterproductive. It can be stated that all measures, which raise the exhaust gas enthalpy in the first phase, support the converters' heat-up.

The subsequent phase, in which the heat transfer coefficient and internal surface area quantitatively control the heat-up, presents advantages for substrates with high cell densities. Another positive aspect of the large internal surface area for high cell density monoliths is the accommodation of more catalytically active sites compared to their low cell density equivalents.

Direct electric heating of monoliths could constitute another promising alternative to shorten the light-off period. In this case, besides the necessity of an electrical conductive substrate, the converters' thermal inertia is the decisive parameter during heat-up.

Author Contributions: The authors' contributions can be divided into: conceptualization, V.S. and L.M.; development of methodology, L.M. and V.S.; software and modelling, V.S. and T.S.; validation, V.S., and L.M.; formal analysis, T.S.; investigation, T.S., D.N. and P.M.; writing—original draft preparation, T.S. and L.M.; writing—review and editing, L.M. and C.P.; visualization, T.S.; supervision, L.M. and C.P. All authors have read and agreed to the published version of the manuscript.

Funding: This research received no external funding.

Informed Consent Statement: Not applicable.

Data Availability Statement: Data is contained within the article.

Conflicts of Interest: The authors declare no conflict of interest.

Abbreviations

Latin Letters

A	area	m^2
a	free edge length	m
c_{mp}	mean isobaric heat capacity	$J \cdot kg^{-1} \cdot K^{-1}$
c_p	isobaric heat capacity	$J \cdot kg^{-1} \cdot K^{-1}$
d	diameter	m
l	length	m
m	mass	kg

$\dot{m}$	gravimetric flow rate	$kg \cdot s^{-1}$
Nu	Nusselt number	-
p	pressure	Pa
Pe	Peclet number	-
Pr	Prandtl number	-
Q	heat	J
$\dot{Q}$	heat flux	W
$\dot{q}$	heat flux density	$W \cdot m^{-2} \cdot K^{-1}$
R_{sp}	specific gas constant	$J \cdot kg^{-1} \cdot K^{-1}$
Re	Reynolds number	-
T	temperature	K
t	time	s
u	velocity	$m \cdot s^{-1}$
UI	uniformity index	-
V	volume	m^3
$\dot{V}$	volumetric flow rate	$m^3 \cdot s^{-1}$
X	conversion	%
Greek Letters		
α	heat transfer coefficient	$W \cdot m^{-2} \cdot K^{-1}$
Δ	difference	-
λ	heat conductivity	$W \cdot m^{-1} \cdot K^{-1}$
η	dynamic viscosity	$kg \cdot m^{-1} \cdot s^{-1}$
ρ	density	$kg \cdot m^{-3}$
Subscripts		
avg	average	
cat	catalytic converter	
c	cell	
$cond$	conductive	
$conv$	convective	
gas	exhaust gas	
$hydr$	hydraulic	
in	inflowing	
int	internal	
ln	logarithmic	
$loss$	heat loss	
$mean$	mean	
$mono$	monolith	
$open$	open	
out	outflowing	
$solid$	solid	
Definitions/Abbreviations		
1D	one-dimensional	
Al_2O_3	aluminum oxide	
CI	compression ignited	
CO	carbon monoxide	
CO_2	carbon dioxide	
cpsi	cells per square inch	
Cu	copper	
DOC	diesel oxidation catalyst	
EGR	exhaust gas recirculation	
Fe	iron	
GHSV	gas hourly space velocity	
GSA	geometric surface area	
HC	hydrocarbons	
ICE	internal combustion engines	
NH_3	ammonia	
NO	nitrogen monoxide	
NO_2	nitrogen dioxide	

NO_x	nitrogen oxides
NSC	nitrogen storage catalyst
NSCR	non-selective catalytic reduction
OFA	open frontal area
Pd	palladium
PM	particulate matter
Pt	platinum
Rh	rhodium
SCR	selective catalytic reduction
SI	spark-ignited
TWC	three-way catalytic converter

Appendix A

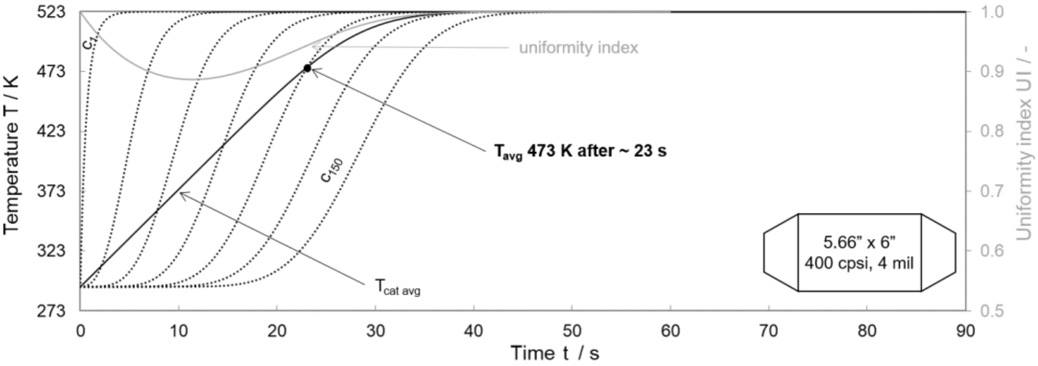

Figure A1. Heat-up of 400 cpsi, 4 mil (reference) at steady state heat-up.

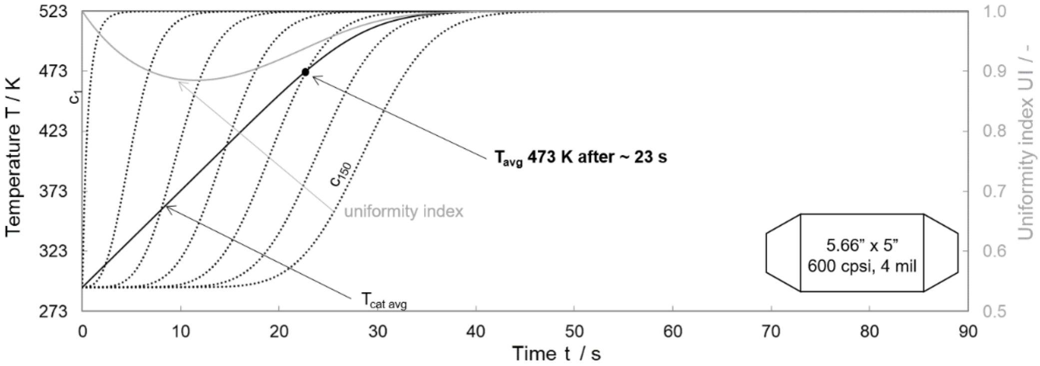

Figure A2. Heat-up of 600 cpsi, 4 mil with reduced length at steady state heat-up.

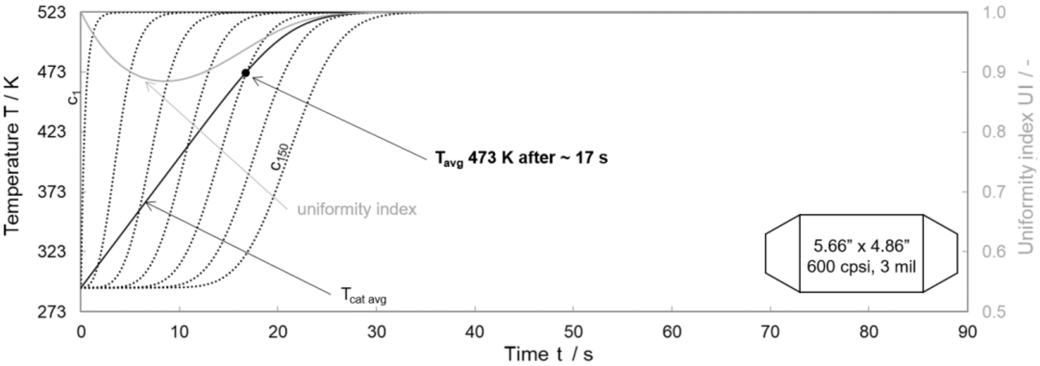

Figure A3. Heat-up of 600 cpsi, 3 mil with reduced length at steady state heat-up.

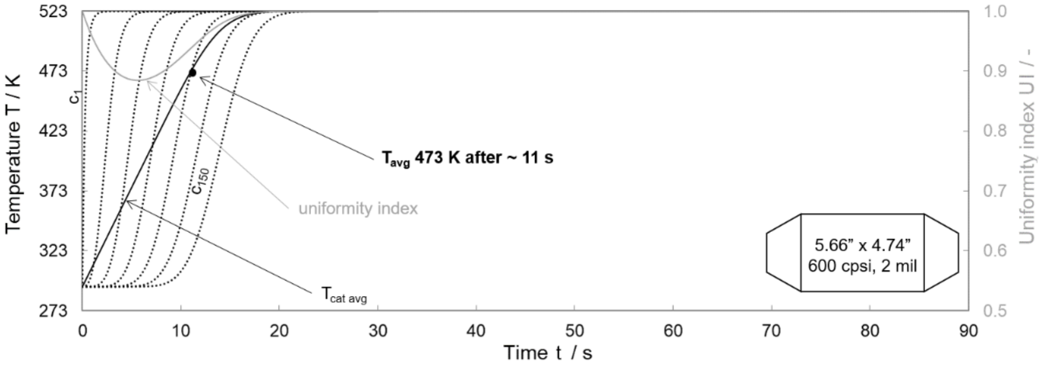

Figure A4. Heat-up of 600 cpsi, 2 mil with reduced length at steady state heat-up.

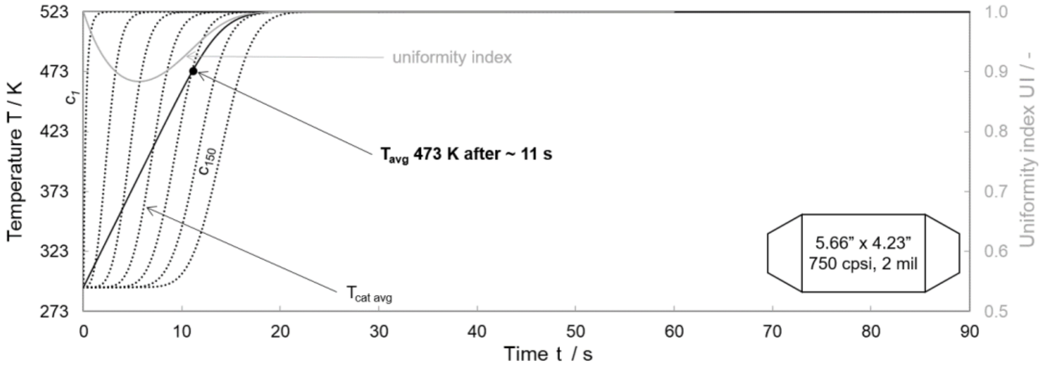

Figure A5. Heat-up of 750 cpsi, 2 mil with reduced length at steady state heat-up.

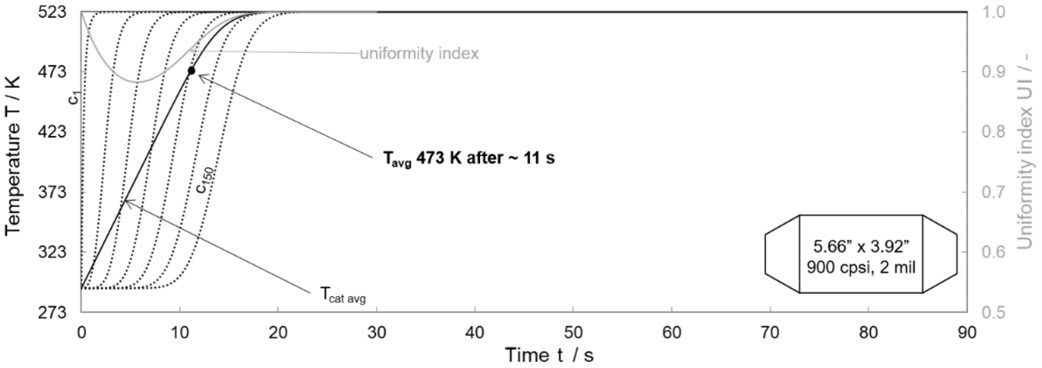

Figure A6. Heat-up of 900 cpsi, 2 mil with reduced length at steady state heat-up.

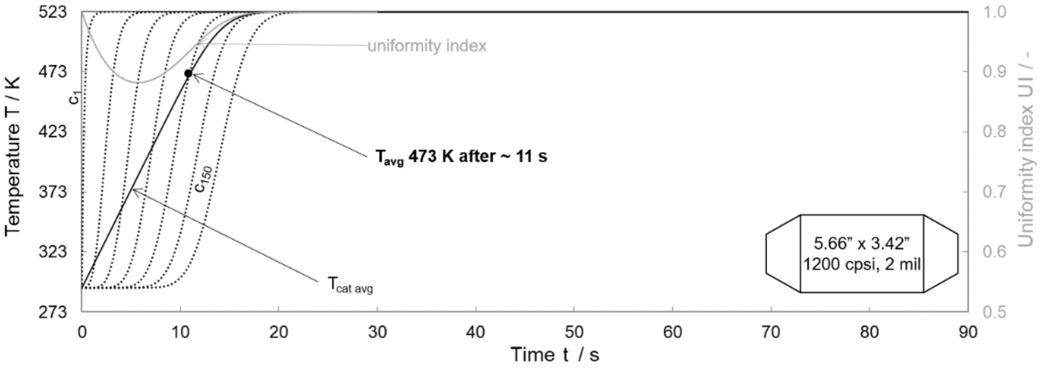

Figure A7. Heat-up of 1200 cpsi, 2 mil with reduced length at steady state heat-up.

References

1. Moeltner, L.; Hohensinner, M.; Schallhart, V. Experimental and Numerical Analysis of Low Temperature NO_x—Conversion in Urban Busses. In *SAE Technical Paper Series*; SAE International: Warrendale, PA, USA, 2016. [CrossRef]
2. Bresch-Pietri, D.; Leroy, T.; Petit, N. Control-oriented Time-varying Input-delayed Temperature Model for SI Engine Exhaust Catalyst. In Proceedings of the 2013 American Control Conference, Washington, DC, USA, 17–19 June 2013; pp. 2189–2195.
3. Sabatini, S.; Kil, I.; Dekar, J.; Hamilton, T.; Wuttke, J.; Smith, M.A.; Hoffman, M.A.; Onori, S. A New Semi-Empirical Temperature Model for the Three Way Catalytic Converter. *IFAC-PapersOnLine* **2015**, *48*, 434–440. [CrossRef]
4. Chang, H.-L.; Chen, H.-Y.; Koo, K.; Rieck, J.S.; Blakeman, P. Gasoline Cold Start Concept (gCSC™) Technology for Low Temperature Emission Control. *SAE Int. J. Fuels Lubr.* **2014**, *7*, 480–488. [CrossRef]
5. Basshuysen, R. *"Handbuch Verbrennungsmotor" ATZ/MTZ Fachbuch*, 8th ed.; Springer: Berlin, Germany, 2017; ISBN 978-3-658-10901-1.
6. Schallhart, V.; Moeltner, L. Effect of Spray-Exhaust Gas Interactions on Ammonia Generation in SCR Mixing Sections. *SAE Int. J. Fuels Lubr.* **2018**, *11*, 181–200. [CrossRef]
7. Moeltner, L.; Hohensinner, M.; Schallhart, V. Aging Effects of Catalytic Converters in Diesel Exhaust Gas Systems and Their Influence on Real Driving NOx Emissions for Urban Buses. *SAE Int. J. Commer. Veh.* **2018**, *11*, 171–190. [CrossRef]
8. Marsh, P.; Acke, F.; Konieczny, R.; Brück, R.; Hirth, P. Application Guideline to Define Catalyst Layout for Maximum Catalytic Efficiency. In *SAE Technical Paper Series*; SAE International: Warrendale, PA, USA, 2001. [CrossRef]
9. Gulati, S.T. Design Considerations for Advanced Ceramic Catalyst Supports. In *SAE Technical Paper Series*; SAE International: Warrendale, PA, USA, 2000. [CrossRef]
10. Gottschalk, W.; Kirstein, G.; Magnor, O.; Schultalbers, M.; Wetten, R. Investigations on a Catalyst Heating Strategy by Variable Valve Train for SI Engines. *SAE Int. J. Engines* **2012**, *5*, 1177–1200. [CrossRef]
11. Szolak, R.; Danckert, B.; Susdorf, A.; Beutel, P.; Pautsch, K.; Ewert, C.; Rümmele, F.; Kakadiya, A.; Schaadt, A. *CatVap®—A New Heating Measure for Exhaust Aftertreatment System*; Springer Viewag: Wiesbaden, Germany, 2020; pp. 37–52.
12. Holy, G.; Bruck, R.; Hirth, P. Improved Catalyst Systems for SULEV Legislation: First Practical Experience. In *SAE Technical Paper Series*; SAE International: Warrendale, PA, USA, 2000.
13. Gelner, A.D.; Pastoetter, C.; Beck, H.A.; Härtl, M.; Wachtmeister, G. Fuel Dosing on a Diesel Oxidation Catalyst for After-Treatment System Heating on a Heavy-Duty Engine Powered by Polyoxymethylene Dimethyl Ethers. In *SAE Technical Paper Series*; SAE International: Warrendale, PA, USA, 2020.
14. Della Torre, A.; Montenegro, G.; Onorati, A.; Cerri, T. CFD Investigation of the Impact of Electrical Heating on the Light-off of a Diesel Oxidation Catalyst. In *SAE Technical Paper Series*; SAE International: Warrendale, PA, USA, 2018. [CrossRef]
15. Breuer, J.; Hirth, P.; Bruck, R.; Kruse, C. Electrically Heated Catalyst for Future USA and European Legislation. In *SAE Technical Paper Series*; SAE International: Warrendale, PA, USA, 1996. [CrossRef]
16. Wiehl, J.; Vogt, C.D. Keramische Ultradünnwandsubstrate für moderne Katalysatoren. *MTZ Mot. Z.* **2003**, *64*, 112–119. [CrossRef]
17. Madhusoodana, C.D.; Das, R.N.; Umarji, A.M.; Panda, P.K.; Kannan, T.S. Thermal Expansion and Thermal Shock Resistance of Cordierite Honeycombs Used in Catalytic Converters. In *SAE Technical Paper Series*; SAE International: Warrendale, PA, USA, 1999. [CrossRef]
18. McLaren, M.G.; Ott, W.R. Ceramic Monolithic Substrates-State of the Art. In *SAE Technical Paper Series*; SAE International: Warrendale, PA, USA, 1974. [CrossRef]
19. Teague, M. Ceramic Substrate Technology for Automotive Catalysts. In *SAE Technical Paper Series*; SAE International: Warrendale, PA, USA, 1976. [CrossRef]
20. Gulati, S.T. Ceramic Converter Technology for Automotive Emissions Control. In *SAE Technical Paper Series*; SAE International: Warrendale, PA, USA, 1991. [CrossRef]
21. Lundsager, C.B.; Turner, G.J.; Pentecost, J.L. Thermoplastics Process for Catalyst Substrates. In *SAE Technical Paper Series*; SAE International: Warrendale, PA, USA, 1976. [CrossRef]
22. Day, J.P. The Design of a New Ceramic Catalyst Support. In *SAE Technical Paper Series*; SAE International: Warrendale, PA, USA, 1990. [CrossRef]
23. Machida, M.; Yamada, T.; Makino, M. Study of Ceramic Catalyst Optimization for Emission Purification Efficiency. In *SAE Technical Paper Series*; SAE International: Warrendale, PA, USA, 1994. [CrossRef]
24. Bach, C.; Eggenschwiler, P.D. Ceramic Foam Catalyst Substrates for Diesel Oxidation Catalysts: Pollutant Conversion and Operational Issues. In *SAE Technical Paper Series*; SAE International: Warrendale, PA, USA, 2011. [CrossRef]
25. Dimopoulos, P.; Bach, C.; Vogt, U.; Herrmann, K. Ceramic Foams as Catalyst Substrates: Pre-catalyst Application Homogenising the Exhaust Flow upstream of Aftertreatment Devices. In *SAE Technical Paper Series*; SAE International: Warrendale, PA, USA, 2007.
26. Jatkar, A.D. A New Catalyst Support Structure for Automotive Catalytic Converters. In *SAE Technical Paper Series*; SAE International: Warrendale, PA, USA, 1997. [CrossRef]
27. Stankiewicz, E.P.; Sherman, A.J.; Zinn, A.A.; Scott, D.J. Properties and Performance of UltraCatTM Open-Cell Silicon Carbide Foam Catalyst Substrates. In *SAE Technical Paper Series*; SAE International: Warrendale, PA, USA, 1998. [CrossRef]

28. Lakshmikantha, M.; Keck, M. Optimization of Exhaust Systems. In *SAE Technical Paper Series*; SAE International: Warrendale, PA, USA, 2002.
29. Pannone, G.M.; Mueller, J.D. A Comparison of Conversion Efficiency and Flow Restriction Performance of Ceramic and Metallic Catalyst Substrates. In *SAE Technical Paper Series*; SAE International: Warrendale, PA, USA, 2001. [CrossRef]
30. Tamura, N.; Matsumoto, S.; Kawabata, M.; Kojima, M.; Machida, M. The Development of an Automotive Catalyst using a Thin Wall (4 mil/400cpsi) Substrate. In *SAE Technical Paper Series*; SAE International: Warrendale, PA, USA, 1996.
31. Aoki, Y.; Miyairi, Y.; Ichikawa, Y.; Abe, F. Product Design and Development of Ultra Thin Wall Ceramic Catalytic Substrate. In *SAE Technical Paper Series*; SAE International: Warrendale, PA, USA, 2002. [CrossRef]
32. Schmidt, J.; Franz, J.; Merdes, N.; Brady, M.J.; Mueller, W.; Lindner, D.; Bog, T.; Clark, D.; Buckel, T.; Stoepler, W.; et al. Utilization of Advanced Three-Way Catalyst Formulations on Ceramic Ultra Thin Wall Substrates for Future Legislation. In *SAE Technical Paper Series*; SAE International: Warrendale, PA, USA, 2002. [CrossRef]
33. Knon, H.; Brenscheidt, T.; Flörchinger, P. Keramische Ultradünnwandträger für zukünftige Emissionsanforderungen. *MTZ Mot. Z.* **2001**, *62*, 662–666. [CrossRef]
34. Twigg, M. Advanced Exhaust Emissions Control—A Selective Review of the Detroit 2000 SAE World Congress. *Platin. Metals Rev.* **2000**, *44*, 67.
35. Tanaka, M.; Nishimura, M.; Murata, M.; Itou, K. The Innovative Reinforcement Technology of Thin Wall Ceramic Substrate Having High Coatability. In *SAE Technical Paper Series*; SAE International: Warrendale, PA, USA, 2000. [CrossRef]
36. Umehara, K.; Makino, M.; Brayer, M.; Becker, E.R.; Watson, R. Prediction of Catalytic Performance for Ultra Thin Wall and High Cell Density Substrates. In *SAE Technical Paper Series*; SAE International: Warrendale, PA, USA, 2000.
37. Lafyatis, D.S.; Will, N.S.; Martin, A.P.; Rieck, J.S.; Cox, J.P.; Evans, J.M. Use of High Cell Density Substrates and High Technology Catalysts to Significantly Reduce Vehicle Emissions. In *SAE Technical Paper Series*; SAE International: Warrendale, PA, USA, 2000.
38. Hirose, S.; Yamamoto, H.; Suenobu, H.; Sakamoto, H.; Katsube, F.; Busch, P.; Martín, A.; Kai, R.; Vogt, C.D. Development of High Porosity Cordierite Honeycomb Substrate for SCR Application to Realize High NOx Conversion Efficiency and System Compactness. *SAE Int. J. Mater. Manuf.* **2014**, *7*, 682–687. [CrossRef]
39. Andreassi, L.; Cordiner, S.; Mulone, V. Cell Shape Influence on Mass Transfer and Backpressure Losses in an Automotive Catalytic Converter. In *SAE Technical Paper Series*; SAE International: Warrendale, PA, USA, 2004. [CrossRef]
40. Day, J.P. Substrate Effects on Light-Off—Part II Cell Shape Contributions. In *SAE Technical Paper Series*; SAE International: Warrendale, PA, USA, 1997. [CrossRef]
41. Shamim, T.; Shen, H. Effect of Geometric Parameters on the Performance of Automotive Catalytic Converters. *Int. J. Sci. Technol.* **2003**, *14*, 15–22.
42. Anderson, M.J. Ultra Thin Wall Mat Design and Optimization with Hybrid Mats. In *SAE Technical Paper Series*; SAE International: Warrendale, PA, USA, 2004. [CrossRef]
43. Maus, W.; Brück, R. The Conical Catalytic Converter and Its Potential for Future Close-Coupled Converter Concepts. In *SAE Technical Paper Series*; SAE International: Warrendale, PA, USA, 1998. [CrossRef]
44. Bonnefoy, F.; De Meyer, J.; Steenackers, P. High Flexibility in Converter Design by Using Modular Block Metallic Substrates. In *SAE Technical Paper Series*; SAE International: Warrendale, PA, USA, 2000. [CrossRef]
45. Kikuchi, S.; Hatcho, S.; Okayama, T.; Inose, S.; Ikeshima, K. High Cell Density and Thin Wall Substrate for Higher Conversion Ratio Catalyst. In *SAE Technical Paper Series*; SAE International: Warrendale, PA, USA, 1999. [CrossRef]
46. Moore, W.J.; Hummel, D.O.; Trafara, G.; Holland-Moritz, K. *Physikalische Chemie*; Walter de Gruyter GmbH: Berlin, Germany, 1986.
47. Kleiber, M.; Joh, R. *"VDI-Wärmeatlas", Verein Deutscher Ingenieure VDI-Gesellschaft Verfahrenstechnik und Chemieingenieurwesen*; Springer: Berlin, Germany, 2006; ISBN 13-978-3-540-25504-8.